nature communications

Article

https://doi.org/10.1038/s41467-025-60967-z

Dimerization and substrate recognition of human taurine transporter

Received: 23 October 2024

Accepted: 9 June 2025

Yimin Zhang[1,2,7], Jiahui Chen[1,2,7], Nanhao Chen[3], Haolin Xiong[1,2], Zhengjiang Zhu[1,4], Dongxue Yang[5] ✉, Jingpeng Ge[6] ✉ & Jie Yu[1,4] ✉

Taurine is a conditionally essential nutrient and one of the most abundant amino acids in humans, with diverse physiological functions. The cellular uptake of taurine is primarily mediated by the taurine transporter (TauT), and its dysfunction leads to retinal regeneration, cardiomyopathy, neurological and aging-associated disorders. Here we determine structures of TauT in two states: the apo inward-facing open state and the occluded state bound with substrate taurine or γ-aminobutyric acid (GABA). In addition to monomer, the structures also reveal a TauT dimer, where two cholesterol molecules act as "molecular glue", and close contacts of two TM5 from each protomer mediate the dimer interface. In combination with functional characterizations, our results elucidate the detailed mechanisms of substrate recognition, specificity and transport by TauT, providing a structural framework for understanding TauT function and exploring potential therapeutic strategies for taurine-deficiency-related disorders.

Taurine (2-aminoethanesulfonic acid) is among the most abundant amino acids in humans and other eukaryotic organisms[1–3], with particularly high concentrations in excitable tissues such as brain, eyes and heart[4]. It has garnered significant attention due to its diverse physiological roles, including osmoregulation, antioxidation, bile acid conjugation, aging and neuronal development[5–8]. Taurine also plays an important role in the central nervous system by functioning as a neurotransmitter, a partial agonist of N-methyl-D-aspartate (NMDA), $GABA_A$ and glycine receptors[9]. Thus, taurine can partially substitute for GABA or glycine by modulating neuronal activity. While taurine biosynthesis gradually decreases with aging, taurine transporter (TauT) is the major transporter that delivers taurine from hepatic cells to circulatory cells[6,10]. Dysfunction of TauT leads to low intracellular taurine levels that induce retinal degeneration[11], cardiomyopathy[12], neurological disorder, muscle weakness and fatigue, and metabolic dysregulation[7,13]. Particularly, TauT has been implicated to be associated with tumor progression and recurrence, and is the potential target for gastric cancer treatment[14–16]. Despite of the fundamental and multiple functions of TauT, the mechanism by which TauT recognizes and transports taurine is still unclear.

TauT belongs to the solute carrier 6 (SLC6) family, also known as the neurotransmitter sodium symporters (NSSs)[17]. The members of the SLC6 family are primarily sodium- and chloride-dependent transporters, including GABA transporter (GAT), serotonin transporter (SERT), dopamine transporter (DAT), norepinephrine transporter (NET), glycine transporter (GlyT) and creatine transporter (CRT). Among the members of the SLC6 family, TauT shares a high sequence similarity with GATs, up to approximately 62%. However, it demonstrates a distinct substrate specificity, showing significantly lower affinity for GABA compared to GATs[18,19]. As a main inhibitory neurotransmitter in the central nervous system, GABA is recognized as a substrate by TauT and transported across the inner and outer blood-retinal barrier[18]. The underlying mechanisms of GABA recognition by TauT and the differences in substrate specificities between TauT and GATs remain largely unknown.

---

[1] Interdisciplinary Research Center on Biology and Chemistry, Shanghai Institute of Organic Chemistry, Chinese Academy of Sciences, Shanghai, China. [2] University of Chinese Academy of Sciences, Beijing, China. [3] Center for Quantitative Biology, Academy for Advanced Interdisciplinary Studies, Peking University, Beijing, China. [4] Shanghai Key Laboratory of Aging Studies, Shanghai, China. [5] Department of Urology, Institute of Urology (Laboratory of Reconstructive Urology), West China Hospital, Sichuan University, Chengdu, Sichuan, China. [6] School of Life Science and Technology, ShanghaiTech University, Shanghai, China. [7] These authors contributed equally: Yimin Zhang, Jiahui Chen. ✉ e-mail: yangdx@scu.edu.cn; gejp@shanghaitech.edu.cn; yujie@sioc.ac.cn

Lipids have been reported to play an important role in modulating the function and regulating the oligomerization of SLC6 family members, such as DAT, SERT and NET[20–23]. Single-molecule imaging and molecule simulation experiments suggested these transporters exhibited diverse quaternary arrangements, from monomers to complex stoichiometries involving multiple subunits[24–27]. While the structures of most members of the SLC6 family have been resolved in a monomeric form[28–35], the cryo-electron microscopy (cryo-EM) structure of NET was recently determined in a homodimeric state[20]. In this dimeric form, cholesterol and phosphatidylinositol 4,5-bisphosphate (PIP2) are bound to the dimer interface, mediating the homodimerization. Given that NET is the only SLC6 family member observed in a lipid-mediated dimeric form, further evidence or structural studies are essential to fully elucidate the roles of lipids in the oligomerization and function of SLC6 family members.

Here, we isolated TauT in detergent micelles or further reconstituted TauT in nanodiscs, and then determined the single-particle cryo-EM structures of TauT in apo and in complex with taurine or GABA, respectively. These structures reveal TauT adopts an inward-open state in its apo form and transitions to an occluded state upon binding with the substrate taurine or GABA in the monomeric form. Our work also uncovers the homodimeric form of TauT, which is exclusively observed in the nanodiscs condition, with two cholesterol molecules facilitating the dimerization. In conjunction with extensive biochemical characterizations, our studies elucidate the mechanisms of substrate recognition by TauT and the molecule basis for differences in substrate specificities between TauT and GAT1. These findings provide structural insights for developing new therapeutic strategies to treat taurine-related pathological conditions, such as retinal degeneration, cardiomyopathy, aging-associated and neurological disorders.

Results

Dimerization of TauT

To explore the molecule basis of substrate recognition mechanism by TauT, we expressed the full-length and wild-type (WT) human TauT in HEK293S *N*-acetyl-glucosaminyltransferase I$^-$ (GnTI$^-$) cells and performed the [^{3}H]-taurine uptake assay using both C-terminal fluorescent-tagged and untagged TauT. The results showed that untagged TauT exhibited a lower Michaelis constant (K_m) value (~ 50 µM) compared to C-terminal fluorescent-tagged TauT (~ 215 µM) (Fig. 1A). Since the transport activity of untagged TauT was more consistent with previously reported values[36,37], it was selected for subsequent transport assays. We prepared the lauryl maltose neopentyl glycol (LMNG)-purified protein or reconstituted LMNG-purified protein into membrane scaffold protein (MSP) 1D1-nanodiscs composed of POPC, POPE and POPG for structural determinations (Supplementary Fig. 1a, b). Under detergent conditions, the majority of classes in two-dimensional (2D) classifications displayed discernible monomeric structural characteristics, yielding a single reconstruction map for both the apo form and in the complex with taurine or GABA at resolutions of 3.20 Å, 3.05 Å and 3.26 Å (Supplementary Figs. 2–4 and Supplementary Table 1), respectively. In the MSP1D1-nanodiscs condition, it was observed that the nanodiscs in certain 2D classes were apparently longer than others, displaying clear secondary structure projections, indicating the presence of multiple oligomeric state within this dataset (Supplementary Fig. 2b). Subsequent three-dimensional (3D) classification revealed that apo-TauT in the nanodiscs adopts two oligomerization states-monomer and dimer, which account for approximately 81% and 18% of the total particles, respectively (Fig. 1C). This finding is consistent with previous single molecule studies showing that monomer constitutes the largest fraction of plasma membrane expressed oligomeric SERT and DAT[24,26]. The cryo-EM maps of the monomeric and dimeric TauT in nanodiscs were determined at resolutions of 3.23 Å and 3.25 Å, respectively (Fig. 1B, D and Supplementary Fig. 2b–e). Notably, the structure of monomeric TauT in nanodiscs is identical to that of TauT in detergent.

In order to investigate whether the nanodiscs components POPC, POPE and POPG artificially induce the formation of dimeric TauT or if the 10 nm size of MSP1D1-nanodiscs restricts the assembly of multimeric TauT, we reconstituted TauT into MSP1D1-nanodiscs composed of brain total lipids (BTL) and into MSPE3D1-nanodiscs with a larger diameter of 12 nm, respectively. We collected one hundred cryo-EM micrographs for each condition and analyzed different states of TauT by 2D classification analysis (Supplementary Fig. 4e–h). The particle fractions of monomeric and dimeric TauT in BTL-MSP1D1 and POPC/POPE/POPG-MSPE3D1nanodiscs were approximately similar to those in POPC/POPE/POPG-MSP1D1nanodiscs (Fig. 1C), suggesting that the composition and size of nanodiscs do not affect the presence of dimeric TauT.

TauT exhibits a distinct homodimeric assembly in comparison with the dimeric NET structure (Fig. 1E, F and Supplementary Fig. 5a–f). Unlike NET, where several cholesterols, phosphatidylinositol (PI) and PIP2 molecules exclusively mediate the dimerization of NET[20], the interface of the TauT homodimer is facilitated by only two cholesterol molecules and close contacts of TM5 from each protomer. It is noteworthy that in NET, cholesterol, PI and PIP2 molecules are packed against TM3, TM4, TM9 and TM12, whereas in TauT, the two cholesterols act as “molecule glue”, wedging between TM5 from one protomer and TM7 as well as EL3 from the other protomer (Fig. 1H, I). These two cholesterols form hydrophobic interactions with residues Leu258, Val259, Val262, Thr266 from TM5; residues Phe338 and Phe342 from TM7; and residue Leu278 from EL3 (Fig. 1G, H). In addition, the hydrophilic head of cholesterol potentially form a polar interaction with Arg263 from TM5. Furthermore, intermolecular contacts are mediated by hydrophobic interactions between Leu265 and Val262 in TM5 from each protomer (Fig. 1I). Mutating either Val262 or Leu265 to alanine retained partial activity, whereas Val262Arg, Val262Glu, Leu265Arg and Leu265Glu mutants lead a complete loss of TauT activity (Supplementary Fig. 1e, f). These findings indicate that hydrophobic interactions between Val262 and Leu265 play an important role in dimer formation. Further studies are required to elucidate the physiological significance of the dimeric TauT in future research endeavors.

To determine whether increased cholesterol content enhances the fraction of dimeric TauT, we supplemented the nanodisc reconstitution with ~ 10% additional cholesterol. The resulting dimeric TauT fractions (15–20%) were comparable to those observed without supplementation (Fig. 1c), suggesting that added cholesterol does not promote dimerization. To further investigate cholesterol’s role, we removed it using 100 mM methyl-beta-cyclodextrin during purification and performed cryo-EM analysis. After 2D classification, no dimeric TauT with well-defined secondary structure projections was observed (Supplementary Fig. 4e–h), indicating cholesterol is critical for TauT dimerization. In addition, mass spectrometry analysis confirmed that cholesterols co-extracted with TauT during purification in the detergent environment (Supplementary Fig. 1g). Based on these findings, we hypothesized that detergent wrapping around TauT likely impedes dimerization, even in the presence of cholesterols. When reconstituted into the nanodiscs, TauT dimerization appears to be cholesterol-mediated but remains in dynamic equilibrium with the monomeric form, likely due to relatively weak TauT-cholesterol interactions.

Consistently, in the presence of substrate taurine, both monomeric and dimeric TauT are observed, with their structure resolved at resolutions of 3.23 Å and 3.98 Å, respectively (Supplementary Figs. 3b, 6a, b). Two cholesterol molecules are observed and positioned at the dimer interface, as in the dimeric apo-TauT (Supplementary Fig. 6b). Importantly, in both the apo and taurine-bound states, the structure of each protomer in the TauT homodimer is identical to that of the

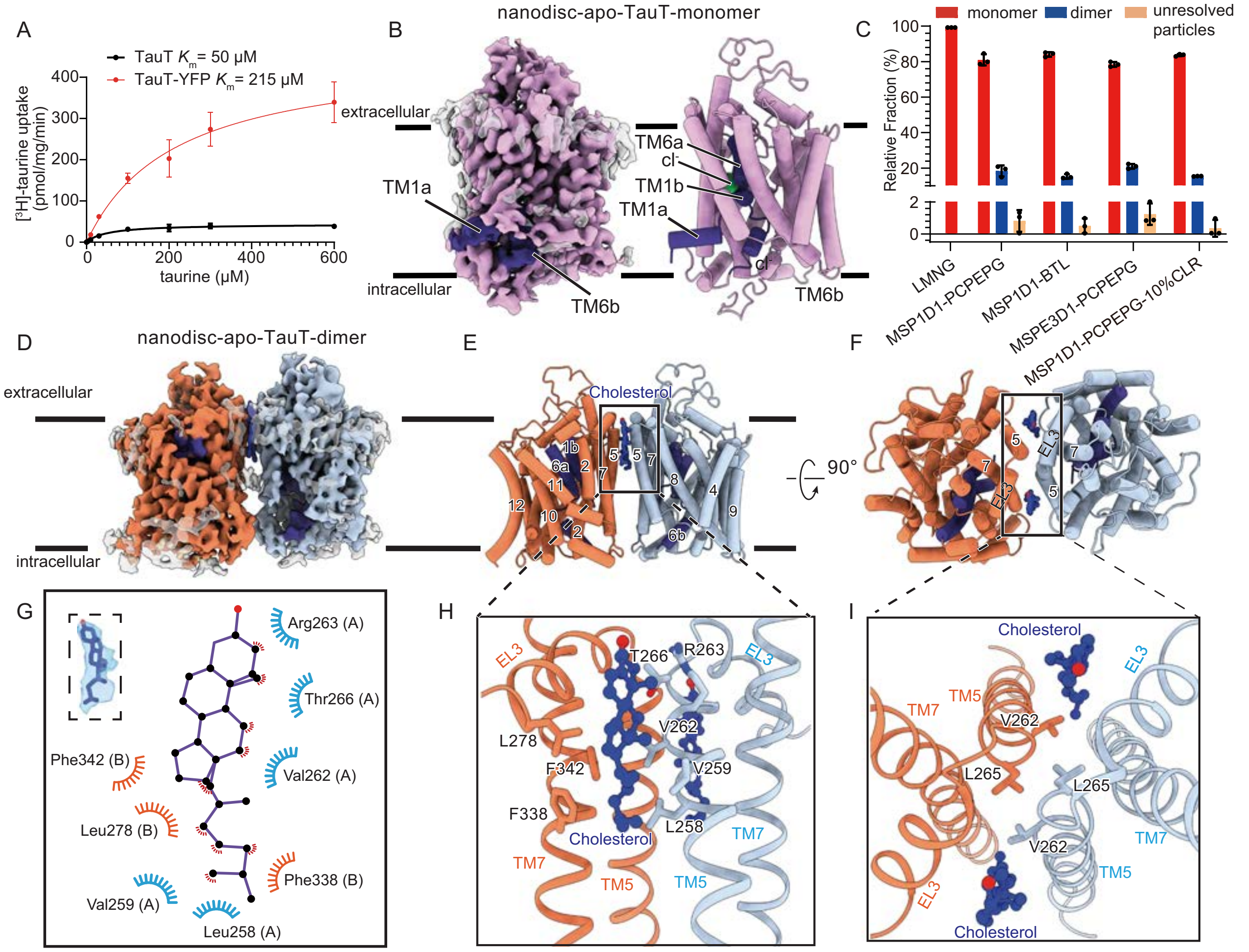

Fig. 1 | Functional characterization and architectures of monomeric and dimeric TauT in nanodiscs. **A** Plots of the ^{3}H-taurine uptake assay for WT human TauT with C-terminal tag (TauT-YFP) and without any tag (TauT). Symbols show the mean derived from $n = 3$ independent biological replicates, each performed in triplicate measurements. Error bars represent the standard deviations (SD). **B** Three-dimensional reconstruction and model of monomeric apo-TauT in nanodiscs. Partially transparent densities represent lipids. **C** Fractions of TauT particles in monomer, dimer and unsolved classes in the detergent micelles (LMNG), MSP1D1-POPC/POPE/POPG (PCPEPG)-nanodiscs, MSP1D1-brain total lipids (BTL)-nanodiscs, MSPE3D1-PCPEPG-nanodiscs and MSP1D1- PCPEPG-nanodiscs supplemented with ~10% additional cholesterol (MSP1D1_PCPEPG_10% CLR). Each point is mean ± SD. from three independent experiments, each with a single measurement ($n = 3$). **D**–**F** Cryo-EM map (**D**) and structures (**E**, **F**) of dimeric apo-TauT in nanodiscs viewed parallel to the membrane (**D**, **E**) and viewed from the extracellular side (**F**). Two gating helices, TM1 and TM6, are in dark blue and two cholesterols are in ball and stick representation. **G** Schematic showing the cholesterol-protein interactions generated from the LigPlot[62,63]. The inset shows the densities of cholesterol. **H**, **I** The enlarged views of the dimer interface mediated by cholesterols (**H**) and close contacts of two TM5 from each protomer (**I**). Key residues are shown in sticks.

monomeric TauT in both the nanodiscs and detergent micelles environments. Nevertheless, there are missing densities for TM1a and ions in the apo-TauT dimer, as well as for the substrate and ions in the taurine-TauT dimer these may be attributed to the relatively lower map quality of TauT homodimer. The structure of TauT complexed with GABA was only determined in detergent micelles, as we expected it to yield similar results to the TauT complexed with taurine in the nanodiscs condition. Because detergent conditions produced higher quality maps with well-defined densities for all the transmembrane helix, extracellular and intracellular loops, substrate and ions, the following structural analysis was performed on the TauT structures in detergent micelles unless otherwise indicated.

Overall structure of TauT

The overall architecture of TauT adopts a canonical LeuT fold[38], akin to other neurotransmitter members of SLC6. TauT comprises 12 transmembrane helices (TMs), in which TM1-5 and TM6-10 exhibit an inverted pseudo two-fold symmetry. In particular, the non-helical segments in TM1 and TM6 breaks them into two halves (TM1a/1b and TM6a/6b) and are vital to the binding of substrates and inhibitors, as well as the coordination of Na$^+$ and Cl$^-$ (Fig. 2A). The cryo-EM density maps allow us to unambiguously assign 12 TMs, intracellular and extracellular loops and part of the regions of N and C termini both located at the cytoplasmic side (Supplementary Fig. 3c). TauT has three predicted glycosylation sites-Asn163, Asn179, and Asn190, but glycosylation density is observed and modeled only at Asn190. In the extracellular loop connecting TM3 and TM4 (EL2), a highly conserved disulfide bond formed between Cys162 and Cys173 is clearly resolved. However, residues 181–187 in EL2 could not be modeled due to relatively weak densities. One reported phosphorylation site[39], Ser322, is resolved on the end of TM7. The cryo-EM map also allows us to assign the densities of Na$^+$, Cl$^-$ and waters for all structures determined in detergent micelles. Among the members of the SLC6 family, TauT shares the highest sequence similarity with GAT1 (~52%). Superimposition of apo-TauT and apo-GAT1 (PDB code: 7Y7V) structures reveals a conserved overall architecture, with an RMSD of 0.9 Å, indicating a high degree of structural similarity. The major structural differences are concentrated on the N- and C-terminal regions

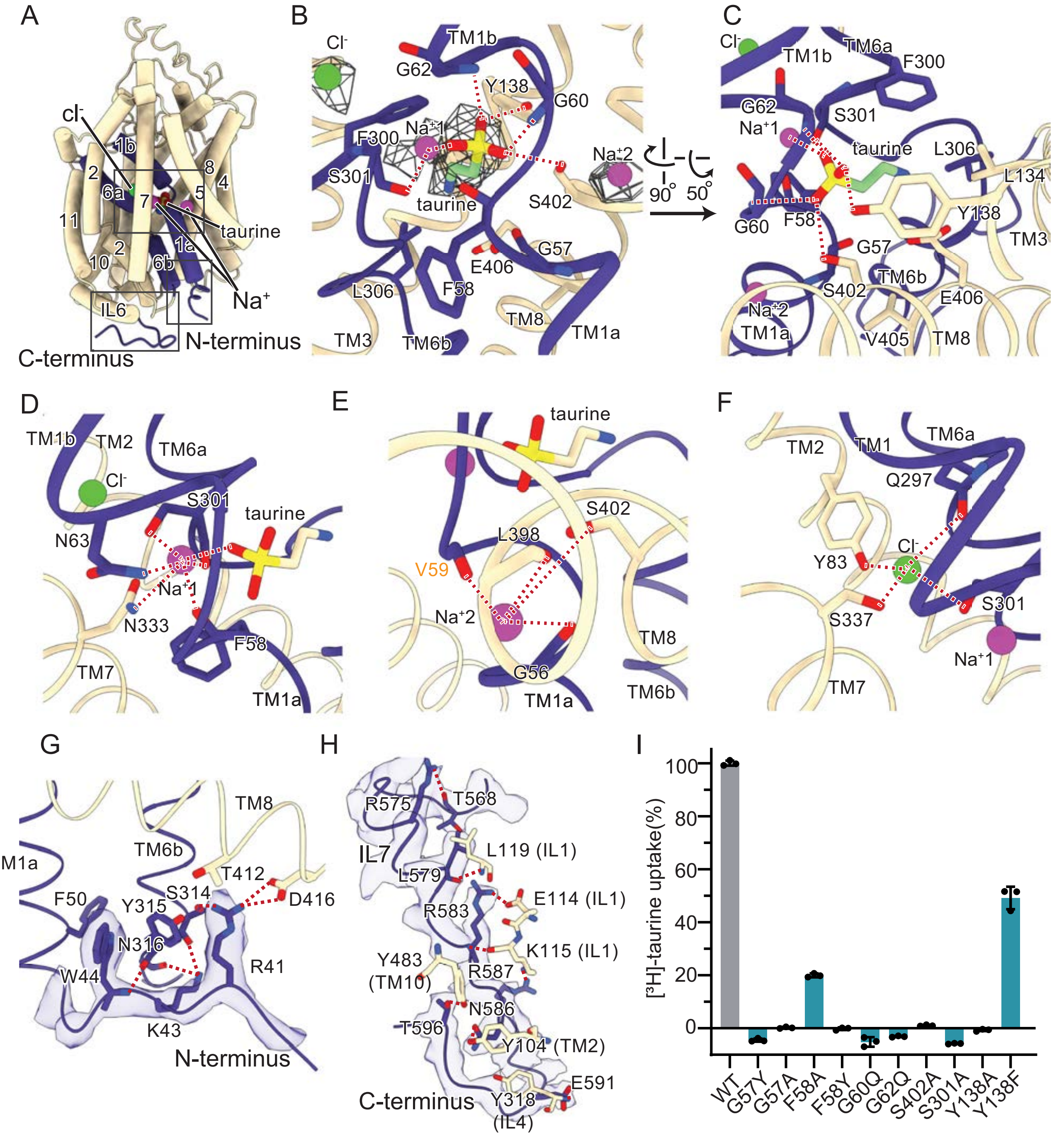

Fig. 2 | The structure of taurine-bound TauT in the occluded state. A Overall structure of TauT. N terminus, C terminus, TM1-12, taurine and ions are labeled. TM1, TM6, N terminus and C terminus are in blue colors. **B**, **C** Recognition of taurine by TauT. The densities for taurine, Na1, Na2 and Cl⁻ are represented in mesh. The surrounding interaction residues are shown in sticks. **D**–**F** Coordinations of Na1 (**D**), Na2 (**E**) and Cl⁻ (**F**) ions. Potential hydrogen bonds are represented in red dash lines. **G**, **H** Detailed views of the extensive interactions in the N terminus (**G**) and C terminus (**H**). Cryo-EM densities for N terminus and C terminus are shown in partially transparent surface. The critical residues are indicated and labeled. **I** The relative uptake activities of the WT TauT and the indicated mutants to explore the importance of the residues involved in coordinating with taurine and ions. Each point is mean ± SD. from three independent experiments, each with a single measurement (*n* = 3).

(Supplementary Fig. 5g–i), likely due to their intrinsic flexibility, a characteristic feature among SLC6 transporters. A key shared structural feature between TauT and GAT1 is the unwound region in TM10, which results from a single-residue insertion (Ser464 in TauT) (Supplementary Fig. 5g, j, k). This insertion induces the formation of a π-helix, modifying the local helical geometry and narrowing the entry pathway, thereby influencing substrate selectivity[40]. Notably, this π-helix is a unique feature found in GATs, TauT and creatine transporters (CRT) within the SLC6 family and is absent in other members (Supplementary Fig. 5k). These structural adaptations may play a crucial role in defining the substrate specificity and transport mechanism of TauT.

The taurine-bound occluded state of TauT

In the structure of taurine-bound TauT (tau-TauT), the extracellular gate is blocked by a close packing surrounding the conserved

NVWRFPY motif of TM1, and TM1a occludes the intracellular permeation pathway (Supplementary Fig. 6d). Similar to the GABA-bound GAT1 (PDB code: 7Y7W) in the inward-occluded conformation[41], the Cα-Cα distance between extracellular gatekeeper residue Arg66 and Asp459 is 9.2 Å (Supplementary Fig. 6e), and the intracellular half helix of TM5 is partially unwounded because of the conserved GlyX9Pro motif[42]. These observations suggest that tau-TauT is in the inward-occluded state.

The central pocket, where taurine and ions bind, is primarily surrounded by the residues from TM1, TM3, TM6 and TM8 (Fig. 2B, C). An evident electron density was observed for taurine. Extra densities for two Na$^+$ and one Cl$^-$ were also observed in the conserved binding sites that present in the structures of GlyT, GAT1, DAT, SERT and NET[29,31,34,41,43]. Based on the extensive coordination with surrounding residues for each density, we identify these extra densities as Na1, Na2 and Cl$^-$, respectively. The Na1 ion, located adjacent to the taurine, is hexagonally coordinated with sulfate oxygen of taurine, side chains of Asn66, Asn333, Ser301, and carbonyl oxygens of Phe58 and Ser301(Fig. 2d). The Na2 ion, positioned farther from taurine, forms four coordination bonds with residues from TM1 and TM8, including Gly56, Val59, Leu398 and Ser402 (Fig. 2E). The Cl$^-$ ion is chelated by the side chains of Tyr83, Gln297, Ser301 and Ser337 (Fig. 2F). Consistent with structural observations, mutating either Tyr83 or Gln297 to alanine results in a complete loss of TauT activity (Supplementary Fig. 1e, f), supporting the notion that transport activity of TauT is Cl$^-$ dependent[44].

In our inward-occluded state of tau-TauT, we have observed well-defined densities for regions of both the N-terminus and C-terminus, enabling us to confidently construct these regions. Specially, Arg41, Lys43, and Trp44, situated on the N-terminus, are involved in multiple interactions with residues in TM8 and TM6 (Fig. 2G), effectively obstructing the passage of substrates and ions into the cytoplasm. In particular, the highly charged side chain of Arg41 forms potential hydrogen bonds with two carboxylate oxygens of Asp416 and the hydroxyl group of Ser314. In addition, it engages a possible cation-π interaction with the aromatic ring of Tyr315. The side chain of Lys43 forms potential hydrogen bonds with carbonyl oxygens of Ser314 and Asn316, while the nitrogen atom in Trp44 backbone interacts with carbonyl oxygen from Tyr315 backbone through a hydrogen bond formation. Substituting the strictly conserved Arg41 and Trp44 with alanine resulted in a complete loss of function, whereas the Lys43Ala mutant displayed significantly decreased transport activity (Supplementary Fig. 1e, f). These findings suggest that interactions mediated by the N-terminal loop are crucial for the transport gating mechanism of TauT, as well as potentially other neurotransmitter transporters within the SLC6 family[28,43].

Intense interactions at the intracellular C-terminus of tau-TauT were observed, which are not defined in other members of the SLC6 family. A short C-terminal helix and a 180° curved C-terminal loop engage in the interactions with TM2, IL1 (connecting TM2 and TM3), IL4 (connecting TM6 and TM7), TM10 and TM12 (Fig. 2H). The connection between C-terminus and TM12 is further reinforced by a hydrogen bonding between side chain of Arg575 and carbonyl oxygen of Thr568. Leu579, Arg583, Asn586, Arg587, Glu591 and Thr596 in the C-terminus of TauT form multiple hydrogen bonds with Leu119 (IL1), Glu114 (IL1), Lys115 (IL1), Tyr104 (TM2), Tyr318 (IL4) and Tyr483 (TM10). These interactions stabilize the position of the C-terminal helix and loop near IL1, IL4, and the intracellular faces of TM2 and TM10. We tested a C-terminal truncated form of TauT (Δ571-620) and found that it exhibited similar K_m to WT, but with an apparent decreased thermal stability (Supplementary Fig. 1c, d), suggesting the extensive interactions observed between the C-terminus and other regions of TauT potentially contribute to stabilizing the overall conformation of TauT.

Taurine binding site

The sulfate group of taurine donates the main interactions with TauT, proximity to the non-helical segment of TM1 and TM6 in the central pocket (Fig. 2B, C). Three oxygen atoms of the sulfate group form multiple potential hydrogen bonds with surrounding residues in the central binding pocket. Specifically, one sulfonyl oxygen forms possible hydrogen bonds with the main chain nitrogen atom of Gly62 and the hydroxyl group of Tyr138, and the other sulfonyl oxygen interacts with the main chain nitrogen atoms of Gly60 and the hydroxyl group of Ser402 through forming possible hydrogen bonds. Substitution of Gly60 and Gly62 with glutamine, alanine or threonine markedly abolished the transport activity of TauT (Fig. 2I and Supplementary Fig. 1e, f), consistent with previous studies that these highly conserved glycine residues in the non-helical segment of TM1 are important for accommodation of the varied substrate size[28,33,45]. Furthermore, replacement of Ser402 with alanine also leads to the abolishment of transport activity (Fig. 2I), supporting the structural observation that it directly interacts with taurine. The hydroxyl oxygen of the sulfate group coordinates with Na1 to bridge the interaction between the hydroxyl oxygen of the sulfate group and Ser301. In line with this observation, the transport activity of the Ser301Ala mutant is completely destructed (Fig. 2I). The highly conserved Tyr138 is vital for the substrate recognition and binding of TauT, with its hydroxyl group coordinating with taurine's sulfonic acid group and its aromatic ring coordinating with the taurine's amino group. Consistently, substitution of Tyr138 with phenylalanine and alanine resulted in a 50% reduction and complete loss of function, respectively (Fig. 2I).

Two residues, Gly57 and Phe58, which are unique to TauT among the members of the SLC6 family and bacterial transporters LeuT and MhsT (Supplementary Fig. 7), play a critical role in the function of TauT. While Gly57 does not appear to interact directly with taurine, its location at the entrance of the central pocket suggests it likely functions as an intracellular gate (Fig. 2C). Supporting this hypothesis, mutating Gly57 to either tyrosine or alanine results in a complete loss of function (Fig. 2I). Phe58, which corresponds to alanine in other neurotransmitter members of SLC6 family, has its carbonyl oxygen potentially engaging in van del Waals interactions with two oxygen atoms of taurine at distances of 3.2 Å and 3.4 Å, respectively. Mutation Phe58 to alanine deceased the transport activity to 20% of WT, and increased K_m to 166.2 μM, suggesting Phe58 is involved in substrate recognition and transport (Figs. 2I and 3C). Nevertheless, substitution of Phe58 with tyrosine caused a complete abolishment of the function. We hypothesize that the hydroxyl group of tyrosine may introduce a steric clash with surrounding residues during the opening of the intracellular gate.

The GABA-bound occluded state of TauT

TauT is described as an "honorary" GAT because of its low affinity for GABA[19]. GAT1 is the main GABA reuptake transporter in the brain[46]. Competition assay shows that GABA binds to TauT with an IC50 value of 1.30 mM (Fig. 3D), which is significantly higher compared to its binding affinity for GAT1, where the K_m is ~ 27.5 μM[41]. To investigate the recognition mechanism of GABA by TauT and to elucidate the differences in substrate specificities between TauT and GAT1, we determined the structure of GABA-bound TauT in detergent micelles (Supplementary Fig. 4a–d). GABA-TauT structure adopts an inward-occluded conformation, with a root-mean-square deviation (RMSD) value of 0.3 Å when superimposed to the tau-TauT structure. In addition, two Na$^+$ ions and one Cl$^-$ ion occupying the same position were also observed.

The orientation of GABA is analogous to that of taurine, however, the carboxylate group of GABA, which contains two oxygen atoms instead of three, engaging in fewer hydrogen bonding interactions compared to the sulfate group of taurine. Two oxygen atoms in GABA form two potential hydrogen bonds with the nitrogen atoms of Gly60

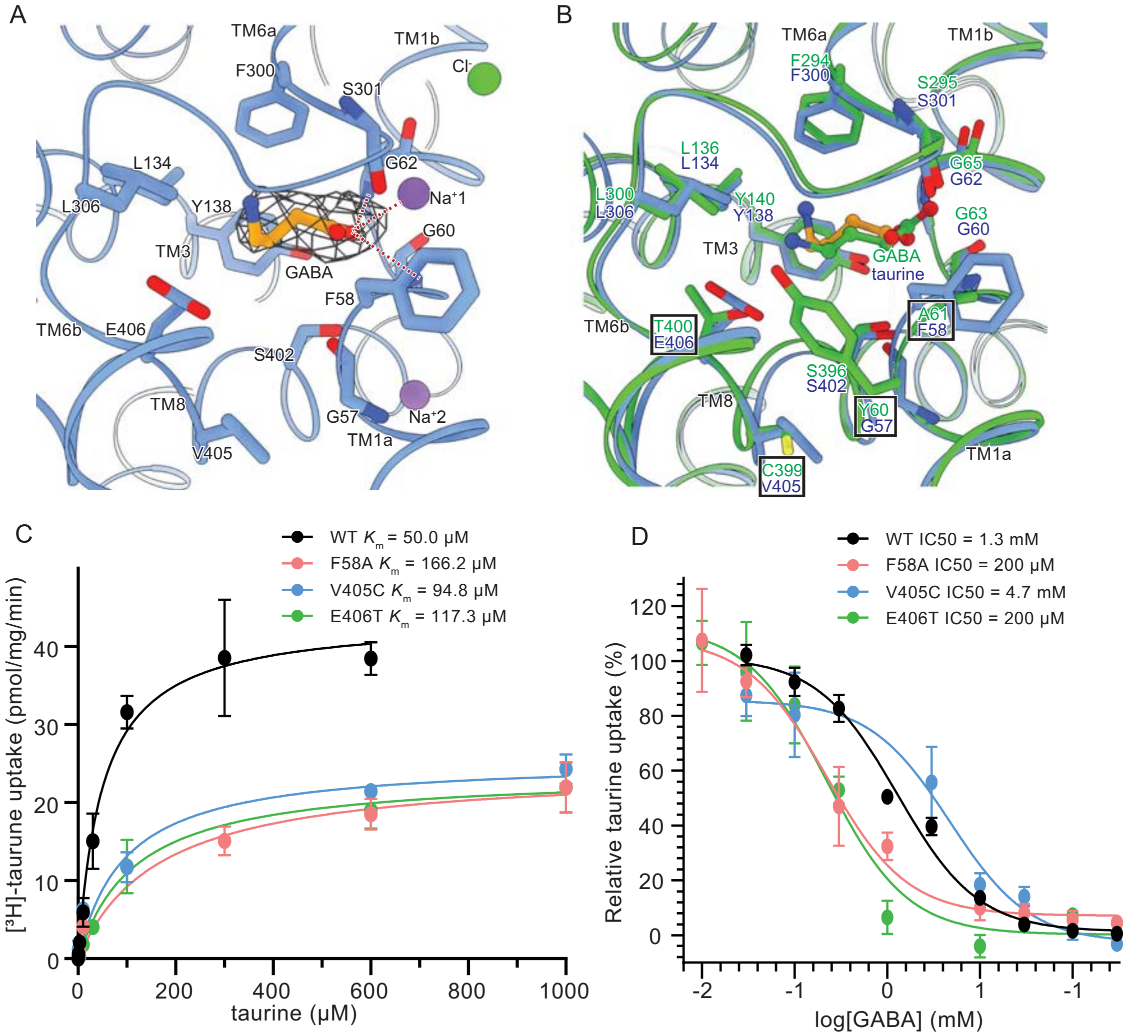

Fig. 3 | Molecular basis for the recognition of GABA by TauT. A Interactions of GABA with residues in the central binding pocket of TauT. The cryo-EM density of GABA is shown in mesh, contoured at 0.6. The key residues and ions are labeled. **B** Superimposition of GABA binding pocket in the TauT (in light blue) and GAT1 (in green, PDB code: 7Y7W) underscores differences in the binding pocket, with an RMSD of 0.85 Å. The different residues are indicated with black squares. **C** Plots of ^{3}H-taurine uptake assay for the WT TauT and the indicated mutants. Symbols are mean ± SD. from three independent experiments, each performed in triplicate measurements. **D** The inhibition curves of the WT TauT and the indicated mutants by GABA in the ^{3}H-taurine uptake assay. Data are presented as mean ± SD from three independent experiments, each performed in triplicate measurements.

and Gly62 (Fig. 3A). In contrast, the three oxygen atoms in taurine form four potential hydrogen bonds with surrounding residues, which might explain the lower binding affinity of GABA compared to taurine. The amino group of GABA engages in interactions with TauT that are similar to those of the amino group of taurine.

To identify the key residues responsible for determining the substrate specificities between TauT and GAT1, we superimposed the binding pockets of GABA-TauT and GABA-GAT1 (PDB code: 7Y7W) (Fig. 3B), with an RMSD value of 0.85 Å. As a result, we found that most residues coordinating the binding of GABA are identical in both structures, with the exception of four residues: Gly57, Phe58, Val405 and Glu406 in TauT, which correspond to Tyr60, Ala61, Cys399 and Thr400 in GAT1, respectively. Those four residues share low conservation across the members of the SCL6 family (Supplementary Fig. 7). As we have described earlier, the Gly57Tyr mutant displays no detectable activity. We mutated Phe58, Glu406 and Val405 in TauT to the corresponding residues in GAT1, and measured the IC50 for those mutants. Remarkably, both the Phe58Ala and Glu406Thr mutants show decreased taurine uptake activity with higher K_m values, but display six-fold lower IC50 values for GABA (Fig. 3D), suggesting that these mutants gained higher binding abilities to GABA. The mutant Val405Cys exhibits reduced transport activity for taurine and a lower binding ability for GABA, as indicated by higher IC50 values. These findings indicate that Phe58 and Glu406 are the key determinants for distinct substrate specificities between TauT and GAT1.

Comparison of the inward and occluded states of TauT

The cryo-EM reconstruction reveals that TauT in the absence of substrate (apo-TauT) is in an inward-open state, in which the extracellular gate is closed and central pocket is solely accessible from the intracellular side (Fig. 4A and Supplementary Fig. 6c). In this state, TM1a splays out towards the membrane, resulting in an open intracellular permeation pathway to the cytoplasm. The dynamic behavior of TM1a has been implicated in other members of SLC6 and the bacterial transporter LeuT[38,47]. Consistently, structural comparisons show that TM1a unwinds with distinct orientations relative to the membrane plane in apo-states, including those of TauT, GAT1, GlyT1, and SERT (Supplementary Fig. 8). While two Na$^+$ ions densities are absent, a strong density of Cl$^-$ ion remains in the structure (Fig. 4A, B), an observation that has also been described in GAT1[41].

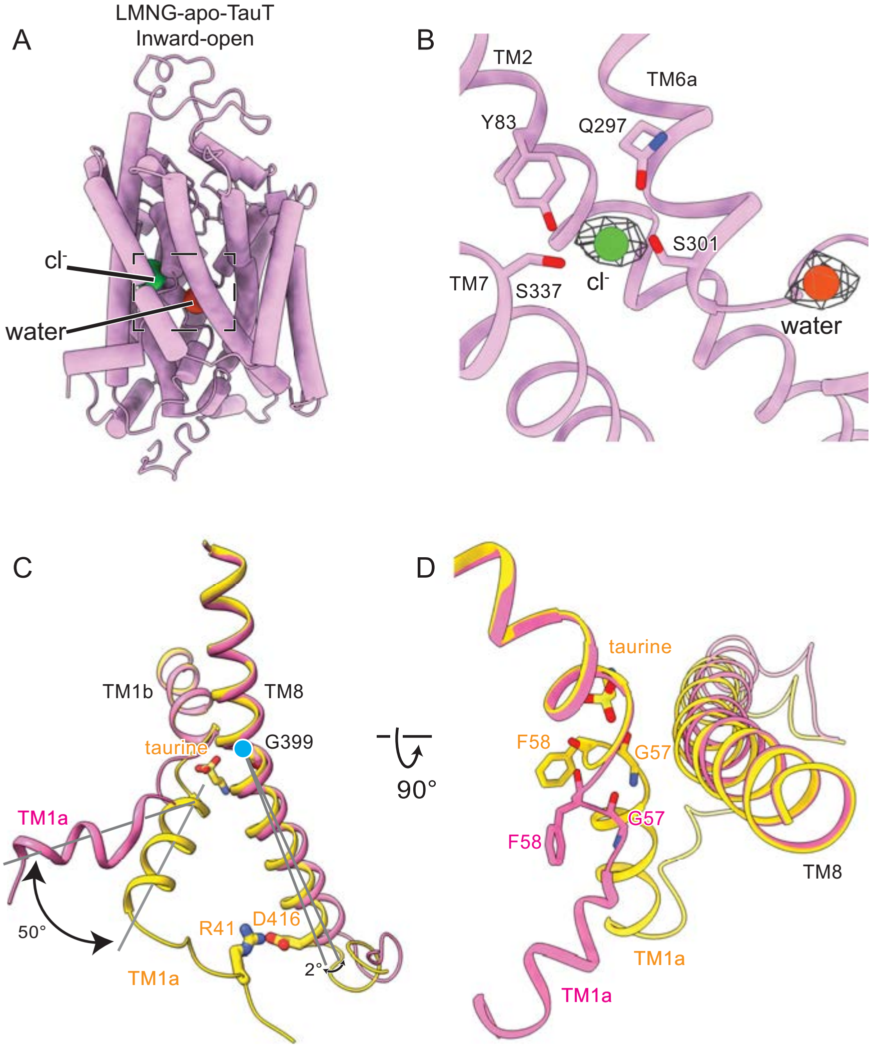

Fig. 4 | Structural comparison of the apo inward-open and taurine-bound occluded states of TauT. A Overall structure of the apo-TauT in the inward-open state. Water and chloride ions are shown in spheres. **B** The detailed view of the coordination of chloride in the apo-TauT. Densities for chloride and water are represented in mesh. **C**, **D** Superimposition of the apo inward-open (pink) and taurine-bound occluded (yellow) states of TauT. The Cα atom of G399 is represented as spheres. The critical residues involved in conformational changes are shown in sticks and labeled.

Superimposition of the structures of apo-TauT and tau-TauT revealed the most significant structural changes occurs in the vicinity of the intracellular gate (Fig. 4C). TM1a bends towards the membrane with a displacement of approximately 50°, disrupting the interactions between its N terminus and TM8, and TM6 that are present in the occluded state. For example, the hydrogen bond between Arg41 and Asp416 (TM8) is disrupted (Fig. 4C), facilitating access to the central site from the cytoplasmic side. In the apo-TauT, the two non-conserved Gly57 and Phe58 in TM1a shift away from the central pocket, thereby opening the permeation pathway from the central pocket to the cytoplasm (Fig. 4D). Consistent with these changes, a water molecule was observed occupying the position of taurine in apo-TauT (Fig. 4A, B). The movement of TM1a is accompanied by a displacement of cytoplasmic half of TM8 with a rotation of 2° towards the membrane (Fig. 4C). The highly conserved pivot residue, Gly399, in the middle of TM8, maintains an unchanged extracellular half of TM8 during its transition from the occluded to the inward conformation, resulting in a constriction at the extracellular surface. In addition, mutating Gly399 to either valine or glutamine completely abolishes the TauT activity (Supplementary Fig. 1e, f). Consistently, the Gly399-Val mutation has been identified to induce retinal degeneration and cardiomyopathy[12].

Transport mechanism of TauT

A homology model of TauT in the outward-open conformation was constructed based on the SERT (PDB ID: 6DZY). A structural superimposition of the outward-open homology model of TauT with its occluded state suggests that the significant structural rearrangements occur at the extracellular gate. Specifically, TM1b and TM6a undergo substantial displacement of 17° and 18°, respectively, resulting in the closure of the extracellular pathway (Supplementary Fig. 9a). TauT has been reported to transport its substrate along with two Na^+ ions and one Cl^- ion in each cycle[44]. We speculate that, the binding of one substrate, two Na^+ and one Cl^- ions in the central site promotes the transition from an outward to an occluded state (Supplementary Fig. 9b). In the occluded state, two unique residues Phe58 and Gly57 are positioned at the entrance of the intracellular permeation pathway, determining the substrate specificity of TauT and preventing the release of substrate and ions (Supplementary Fig. 9c). Upon the substrate is released, Phe58 and Gly57 swing away from the central pocket, allowing the release of substrate and two Na^+ ions to the cytoplasmic side and influx of water into the central pocket in the inward-open state (Supplementary Fig. 9d). This process is facilitated by the significant displacements of TM1a and the intracellular half of TM8. Notably, the Cl^- ion remains bound to the transporter from the occluded to the inward-open state, similar to what

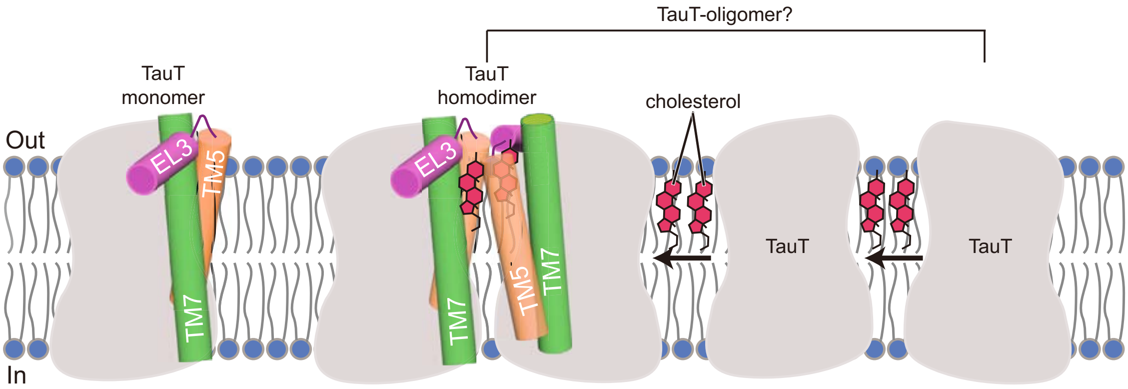

Fig. 5 | Models of the cholesterol-mediated oligomeric assembly of TauT. It is proposed that TauT tends to form multiple oligomeric states, facilitated by the cholesterol in the endogenous environment.

has been observed in GAT1[41]. Further studies are needed to clarify the mechanism of Cl^- ion release.

Discussion

In this study, we have uncovered an unexpected assembly of TauT dimer, which exhibits distinct dimer interfaces compared to the homodimeric structure of NET in the SLC6 family. Notably, the dimeric form of TauT was only observed within nanodiscs rather than detergent micelles environment. Although several research groups have reported the structure of monoamine transporters[20,30,34,47–49], only one group has discovered the dimeric NET in the nanodiscs with POPC/POPE/POPG lipid mix. These findings underscore the crucial role of lipids in regulating the oligomerization of transporters. In addition to monomer and dimer, we also observed a small fraction (~ 0.8%) of unresolved particles displaying trimeric and tetrameric projections during 2D classification (Supplementary Figs. 2b, 3b, 4e, f), indicating that these unresolved particles might represent the trimeric and tetrameric forms of TauT. In these 2D projections, each protomer seems to be juxtaposed within the plane of the membrane, with a similar arrangement as in dimeric TauT. The presence of TauT as a monomer, dimer, trimer and tetramer aligns with previous studies showing that SLC6 family members adopt diverse quaternary assemblies, ranging from monomer to various oligomers[21]. Our study suggests that in a native membrane environment influenced by various lipid components and concentrations, these transporters may exist in multiple states, including monomer, dimer and even higher-order oligomers. Cholesterol likely serves as "molecule glue", mediating the oligomeric assembly of these transporters (Fig. 5). Oligomerization has been shown to play an important role in the trafficking of SLC6 family members[50], however, the exact impact of oligomer formation on the physiological transporter function remains elusive. Further studies are required to elucidate the functional and regulatory implications of TauT oligomerization. In addition, previous studies have shown that cellular taurine depletion reduced the transport activity of TauT[51], underscoring the critical role of cholesterol in the TauT function. In recent years, there has been an increasing interest in taurine due to its essential roles in many aspects of human health and disease. Uncovering the atomic details of taurine binding, recognition and transport by TauT will aid in providing a structural framework for understanding TauT function and exploring potential therapeutic strategies for taurine-deficiency-related disorders, such as retinal degeneration and cardiomyopathy. In addition, this research will contribute to the design of potential therapeutic interventions for tumors, including gastric cancer.

Methods

Expression and purification of human TauT

The full-length human *TauT* gene (UniProt code P31641) was cloned into a pEG BacMam vector with a C-terminal 3C protease site, a Yellow Fluorescent Protein (YFP) and a Twin-Strep affinity tag. The construct was expressed using baculovirus-mediated transduction of HEK293S GnTI$^-$ cells[52]. Cells at a density of ~ 3×10^6 cells per mL were infected with 5% (v/v) TauT BacMam virus and subsequently cultured at 37 °C. A final concentration of 10 mM sodium butyrate was added to the medium after 12 h. The cells were collected after another 48 h at 30 °C.

For protein purification, cells were solubilized in buffer containing 20 mM Tris pH 8.0, 150 mM NaCl, 1% (w/v) n-dodecyl-β-D-maltopyranoside (DDM, Anatrace) and 0.2% (w/v) cholesteryl hemisuccinate (CHS, Anatrace), 0.8 μM aprotinin, 2 μg/ml leupeptin, 2 mM pepstatin A and 1 mM phenylmethylsulfonyl fluoride for 2 h at 4 °C. Insoluble components were removed by centrifugation at 186,009 × *g* for one hour. The supernatant was filtered through a 0.45 μm polystyrene membrane and incubated with the Strep-Tactin resin for one hour at 4 °C. The resin was washed with buffer A containing 20 mM Tris pH 8.0, 150 mM NaCl and 0.01% (w/v) lauryl maltose neopentyl glycol (LMNG, Anatrace). The protein was eluted by buffer A supplemented with 5 mM desthiobiotin. The elution was digested by 3C protease for 2 h on ice, and then concentrated and subjected to size-exclusion chromatography (SEC) (Superose 6 Increase 10/300 GL column) equilibrated with buffer A. The peak fractions were collected and concentrated for the following nanodisc reconstitution and cryo-EM sample preparations.

Nanodiscs reconstitution

POPC:POPE:POPG lipid mix (3:1:1, Avanti Polar Lipids) or brain total lipid (BTL, Avanti) was prepared in chloroform and dried in a vacuum dessicator under high vacuum overnight. The dried lipid film was resuspended to a concentration of 20 mg/ml in buffer B containing 20 mM Tris pH 8.0, and 150 mM NaCl. TauT protein in buffer A was mixed with MSP1D1 or MSPE3D1 and lipid at a molar ratio of 1:5:200 and incubated for 30 min on ice. Detergent was removed by adding an equal volume of Bio-beads to the sample, followed by gentle agitation for 2 h. The Bio-beads were then replaced with fresh one twice. After replacement, the mixture was incubated overnight at 4 °C. Bio-beads were removed by centrifugation at 3005 × *g* for 1 min, and the sample was subjected to SEC equilibrated with buffer B. The peak fractions were collected and concentrated to 2 mg/ml for cryo-EM sample preparations.

[^{3}H]taurine uptake and kinetic assays

The TauT protein, cloned into the pEG BacMam vector without a C-terminal tag, was used for uptake and kinetic assays. HEK 293T cells were first cultured in 24-well plates and transiently transfected with WT or mutant TauTs when the density reached 70%. The cells were cultured at 37 °C with 5% CO_2 for 12 h before the addition of 2 mM sodium butyrate, and then cultured for an additional 24 h. Before performing the uptake experiments, cells were washed once with prewarmed Krebs buffer (125 mM NaCl, 4.8 mM KCl, 5.6 mM glucose, 1.2 mM $CaCl_2$, 1.2 mM KH_2PO_4, 1.2 mM $MgSO_4$, and 25 mM HEPES pH 7.4) and transport assays were conducted in 200 μl Krebs buffer. Uptake experiments were initiated by adding a mixture of 100 μM unlabeled taurine and 20 nM [^{3}H]taurine (12.9 Ci mmol^{-1}, 0.477 TBq mmol^{-1}, Revvity) for 30 min at room temperature. To determine K_m and V_{max} of the WT TauT and its mutants, a series concentrations ranging from 1 μM to 1 mM were prepared by mixing unlabeled taurine and [^{3}H]taurine at a molar ratio of 5000:1. These mixtures were then added to the Krebs buffer. For the inhibition assay, competitive substrate GABA at various concentrations (ranging from 0.1 mM to 300 mM) was added to the Krebs buffer without preincubation, and the reaction was immediately initiated by the addition of 20 nM [^{3}H] taurine. Reactions were stopped by removing the solutions on ice and washing the cell layer twice with 500 μl ice-cold Krebs buffer. Cells were then lysed in 200 μl Krebs buffer containing 1% Triton X-100 for 30 min. The lysate was centrifugated at 16200 × *g*, and 160 μl supernatant was added to a tube containing 1.5 ml of Ultima Gold XR LSC Cocktail (PerkinElmer). The expression levels of various constructs were determined by fluorescent-detection size exclusion chromatography (FSEC). Radioactivity was measured using a Tri-Carb 5110TR Liquid Scintillation Counter (PerkinElmer). The cell density of each well was determined by protein concentration measured using a BCA protein assay kit (ThermoFisher).

Cell surface expression assay

HEK293F cells were transiently transfected with plasmids of TauT WT and mutants with a C-terminal Flag tag. About 3×10^7 cells were collected after culturing for 48 h and washed twice with 1 mL pre-warmed Krebs buffer. Biotinylation was initiated by treating cells with 1 mL sulfo-NHS-SS-biotin (Glpbio) (0.8 mg/mL in Krebs buffer) at 4 °C for 30 min. The reaction was terminated through washing cells with ice-cold Krebs buffer supplemented with 100 mM glycine and incubating cells in the same buffer for 10 min at 4 °C. Cells were then solubilized in buffer containing 20 mM Tris pH 8.0, 150 mM NaCl, 1% (w/v) DDM, 0.8 μM aprotinin, 2 μg/ml leupeptin and 2 mM pepstatin A for 1 h at 4 °C. Insoluble components were removed by centrifugation, and the supernatant was incubated with the Strep-Tactin resin for 1 h at 4 °C. The beads were washed for three times with ice-cold buffer containing 20 mM Tris pH 8.0, 150 mM NaCl and 0.01% (w/v) LMNG and then suspended using 40 μL wash buffer. Samples were loaded on SDS–PAGE to examine protein expression by western blot analysis. TauT WT and mutants were detected using mouse Anti-Flag-tag (1A8) monoclonal antibody (Bioworlde 1: 10,000 dilution) combined with Goat anti-Mouse IRDye 800CW Secondary Antibody (Licor, 1:10,000 dilution). Na^+/K^+-ATPase was used as a loading control and detected with rabbit Anti-Sodium Potassium ATPase monoclonal antibody (abcam, 1:10,000 dilution) combined with Goat anti-Rabbit IRDye 800CW Secondary Antibody (Licor, 1:10,000 dilution).

FSEC-based thermal-stability assay

C-terminal YFP-tagged WT TauT and C-terminal truncated TauT, lacking the residues 571-620 (TauT-ΔCter), were transfected into HEK293S GnTI$^-$ cells. After 60 h, cells were collected and solubilized with lysis buffer containing 20 mM Tris pH 8.0, 150 mM NaCl, 1% (w/v) DDM and protease inhibitors at 4 °C for 2 h. After removing the cell debris by centrifugation, the supernatants were heated at selected temperatures for 10 min. Denatured proteins were removed by ultracentrifugation at 98,560 × *g* for 20 min. The YFP intensity of TauT proteins was measured by FSEC and normalized to the samples without heat treatment. Data was processed, and melting temperatures (Tm) were determined using GraphPad Prism 9.

LC-MS /MS analysis of cholesterol

Lipids were extracted with a modified MTBE protocol, followed previous publications[53,54]. For lipids in TauT protein, the solution was first diluted to 400 μL with water. Then, 960 μL of the extraction solvent (MTBE: MeOH = 5:1; v/v) was added. The sample was vortexed for 60 s, followed by the 10 min of sonication in a water bath (4 °C). The solution was centrifuged at 845 × *g* for 15 min at 4 °C. The upper organic layer (550 μL) was collected into a new Eppendorf tube. Then, 550 μL of MTBE was added to the left layer for further extraction. The solution was vortexed, sonicated, and centrifuged again. Then, the upper organic layer was collected. The re-extraction process was repeated three times in total to ensure the high extraction efficient and recovery rate. Finally, the pooled organic layer was evaporated with a LABCONCO vacuum concentrator. The dry extract was reconstituted using 100 μL of DCM: MeOH (1:1; v/v) before LC-MS analysis. For cholesterol standard solution (0.3 mg/mL of stock solution in DMSO), 960 μL of the extraction solvent (MTBE: MeOH = 5:1; v/v) was added in 400 μL cholesterol standard solution. The sample was vortexed for 60 s, followed by the 10 min of sonication. The rest procedures were the same as lipid extraction of the TauT protein samples.

All lipidomics analyses were performed using a UHPLC system (1290 series, Agilent Technologies) coupled to a quadruple time-of-flight mass spectrometer (TripleTOF 6600, Sciex, Canada) following the protocol in previous publications[54,55]. Lipid separation was performed on a Phenomenex Kinetex C18 column (particle size, 1.7 μm; 100 mm (length) × 2.1 mm (i.d.)) at 55 °C. Mobile phase A was H2O/ACN (6:4, v/v) with 10 mM HCOONH4, and mobile phase B was IPA/ACN (9:1, v/v) with 10 mM HCOONH4. Lipids were eluted at 0.3 mL/min with a linear gradient of 40 % B (0–1.5 min), 40 % B to 85 % B (1.5–10.5 min), stayed at 85% B (10.5–14.0 min), 85 % B to 100 % B (14.0-14.1 min), stayed at 100% B (14.1–15.0 min), decreased to 40% B within 0.2 min, and stayed at 40 % B for 2.8 min for column equilibrium. LC-MS grade water (H2O), methanol (MeOH), isopropyl alcohol (IPA) and HPLC grade dichloromethane (DCM) were purchased from Honeywell (Muskegon, MI, USA). LC-MS grade acetonitrile (ACN) and HPLC-grade methyl-tert-butyl ether (MTBE) were purchased from Merck (Darmstadt, Germany).

The parameters for Sciex TripleTOF6600 were set as follows: ion source gas 1 (GS1), 60 psi; ion source gas 2 (GS2), 60 psi; curtain gas (CUR), 30 psi; temperature, 600 °C; ionspray voltage floating (ISVF), 5000 V in positive mode; declustering potential (DP), 100 V. Data-dependent acquisition (DDA) method was used for MS/MS acquisition. Each acquisition cycle consists of one rapid TOF MS survey scan (200 ms) followed by the consecutive acquisition of 11 product ion scans (50 ms each). For the TOF MS survey scan, the mass range is from 200 to 2000 Da, and the collision energy (CE) is set as 10 V. For product ion scan, the mass ranges are from 100 to 2000 Da, and the collision energy (CE) is set as 45 ± 25 V. Dynamic background subtraction was applied. Dynamic exclusion is set as 4 s after 2 occurrences to ensure the non-repetitive acquisition of MS/MS spectra from the same ion. All analyses were performed in positive ion mode. The sample injection volume was 2 μL. The data was acquired using Analyst TF Software (Version 1.7.1, Sciex, USA).

For data processing, the cholesterol in purified TauT protein samples were manually identified by checking their exact masses, retention times (RT) and MS/MS spectra with cholesterol standard solution. For cholesterol quantification, the Skyline software (version 22.2.0.351) was used for data analysis at the MS1 level. Raw data files (.wiff) and the cholesterol target list containing exact masses and retention times of precursor ions were imported into Skyline for targeted extraction. The integration range was manually checked and adjusted for accurate quantification. The quantification results were exported and analyzed using GraphPad Prism 9.

Cryo-EM sample preparation and data acquisition

To prepare the TauT complexes with different substrates, TauT in detergent or nanodiscs was incubated with 1 mM taurine or 100 mM GABA for 30 min on ice before the samples were placed onto the grids.

A 4.0 μL sample of TauT was applied to the glow-discharged holey carbon grids (Quantifoil R2/1 Au 200 mesh). The grids were blotted for 3 s with a blot force of 0 under 95% humidity at 8 °C, and then plunged into liquid ethane cooled by liquid nitrogen using a FEI Mark IV cryo-plunge instrument.

Cryo-EM datasets were collected on a 300 kV FEI Titan Krios microscope equipped with a Gatan K3 camera and an energy filter. Images were acquired at a magnification of x81,000 in a super-resolution mode, corresponding to a pixel size of 0.5275 Å. Each micrograph was collected at a total dose of 50 $e^-/Å^2$ with a dose rate of ~ 25 e^-/pixel/s using the EPU software. The defocus range was set from − 0.8 μm to − 1.8 μm.

Cryo-EM data processing

For the apo-TauT in LMNG (lmng-apo-TauT), all processing was completed in CryoSparc v4.5.3[56]. A total of 6319 micrographs were motion-corrected and binned by 2-fold using patch motion correction. The contrast transfer function (CTF) estimation was performed by patch CTF estimation. 406 micrographs with low resolution greater than 5 Å were excluded. Particle picking was performed using blob picker and template picker, followed by several rounds of 2D classification. A total of 2,182,743 particles from 2D classes showing apparent helical features in the micelles were selected to generate the initial model by ab initio reconstruction. The best initial model was used as a good reference for heterogenous refinement alongside with three poor references. After several rounds of heterogeneous refinement, 309,754 particles were kept for non-uniform (NU) refinement and local refinement. The final map of the lmng-apo-TauT was resolved at 3.20 Å evaluated by the gold-standard Fourier shell correlation (FSC) (0.143). Similar procedures were employed to process taurine- or GABA-bound TauT in detergents.

For the apo-TauT in nanodiscs (nanodisc-apo-TauT), 5,788,161 particles were picked by blob picker and subjected to 2D classification, from which dimeric and monomeric TauT were identified and subsequently processed separately. For the monomeric TauT, particles were picked by the blob picker, template picker and topaz picker. Particles were extracted with a box of 240 pixels and Fourier cropped down to 120 pixels. After several rounds of 2D classification, ab-initio reconstruction and heterogenous refinement were performed to obtain good references and particles. As a result, 217,473 particles were employed to NU refinement and local refinement. The final map of the nanodisc-apo-TauT-monomer was resolved at 3.23 Å. For the dimeric form of TauT, particles were extracted with a box of 280 pixels and Fourier cropped down to 140 pixels for subsequent processing. Then 60,594 particles were selected for NU refinement after removal of junk particles by 2D classification and heterogenous refinement (C1 symmetry), resulting in a 3.86 Å map. Noting the apparent C2 symmetry and indistinguishable structural features of the two protomers in the dimer, C2 symmetry was applied for the subsequent image processing. To further improve resolution, seed-facilitated multi-reference 3D classification was conducted. Ultimately, 125,858 particles were retained for NU refinement and local refinement, yielding a 3.25 Å resolution reconstruction determined by the gold standard FSC (0.143). A similar strategy was applied in the data processing of taurine-bound TauT in nanodiscs.

Model building

The initial models of TauT were predicted from AlphaFold2 and fitted into the cryo-EM maps in ChimeraX[57]. The models were then manually adjusted and refined using COOT[58]. A flexible N-terminal (residues 1–45 in lmng-apo-TauT and nanodiscs-apo-TauT-monomer, residues 1–38 in lmng-taurine/GABA-TauT and nanodiscs-taurine-TauT-monomer, residues 1–56 in nanodiscs-apo-TauT-dimer, and residues 1–48 in nanodiscs-taurine-TauT-dimer) and C-terminal (residues 597–620 in lmng-apo/taurine/GABA-TauT and nanodiscs-apo/taurine-TauT-monomer, and residues 567–620 in nanodiscs-apo/taurine-TauT-dimer) regions were not built because of the lack of densities in the map. The ligands and ions were assigned and fitted to the corresponding densities based on the conserved binding sites revealed in previous studies. The final models of all datasets were refined in real space using PHENIX[59] with good stereochemistry as evaluated by the MolProbity score[60]. All the structure figures were prepared using ChimeraX[57] and Pymol[61].

Reporting summary

Further information on research design is available in the Nature Portfolio Reporting Summary linked to this article.

Data availability

The sequence of human TauT is available in the following link: https://www.uniprot.org/uniprotkb/P31641/entry#sequences. The cryo-EM maps and coordinates of lmng-apo-TauT, lmng-taurine-TauT, lmng-GABA-TauT, nanodiscs-apo-TauT-monomer, nanodiscs-apo-TauT-dimer, nanodiscs-taurine-TauT-monomer and nanodiscs-taurine-TauT-dimer have been deposited in the Electron Microscopy Data Bank (EMDB) under accession numbers EMD-61379 [https://www.ebi.ac.uk/pdbe/entry/emdb/EMD-61379], EMD-61385 [https://www.ebi.ac.uk/pdbe/entry/emdb/EMD-61385], EMD-61380 [https://www.ebi.ac.uk/pdbe/entry/emdb/EMD-61380], EMD-61392 [https://www.ebi.ac.uk/pdbe/entry/emdb/EMD-61392], EMD-61393 [https://www.ebi.ac.uk/pdbe/entry/emdb/EMD-61393], EMD-61386 [https://www.ebi.ac.uk/pdbe/entry/emdb/EMD-61386] and EMD-61395 [https://www.ebi.ac.uk/pdbe/entry/emdb/EMD-61395] and in the Protein Data Bank (PDB) under accession codes 9JD3, 9JD9, 9JD4, 9JDG, 9JDJ, 9JDA and 9JDL, respectively. Previously resolved structures used in this study are under the accession codes 7Y7W (inward-open GABA-bound GAT1 structure), 7Y7V (inward-open apo GAT1 structure), 3TT3 (inward-open apo LeuT structure), 7LI8 (inward-open apo SERT structure), 8WFJ (inward-open ALX-5407-bound GlyT1 structure), 8YR2 (outward-open Nisoxetine-bound NET structure) in the PDB. Source data are provided in this paper.

References

1. Lourenco, R. & Camilo, M. E. Taurine: a conditionally essential amino acid in humans? An overview in health and disease. *Nutr. Hosp.* **17**, 262–270 (2002).
2. Ripps, H. & Shen, W. Review: taurine: a "very essential" amino acid. *Mol. Vis.* **18**, 2673–2686 (2012).
3. Lambert, I. H., Kristensen, D. M., Holm, J. B. & Mortensen, O. H. Physiological role of taurine-from organism to organelle. *Acta Physiol.* **213**, 191–212 (2015).
4. Jacobsen, J. G. & Smith, L. H. Biochemistry and physiology of taurine and taurine derivatives. *Physiol. Rev.* **48**, 424–511 (1968).
5. Jakaria, M. et al. Taurine and its analogs in neurological disorders: Focus on therapeutic potential and molecular mechanisms. *Redox Biol.* **24**, 101223 (2019).
6. Baliou, S. et al. Significance of taurine transporter (TauT) in homeostasis and its layers of regulation (Review). *Mol. Med. Rep.* **22**, 2163–2173 (2020).
7. Schaffer, S. & Kim, H. W. Effects and mechanisms of taurine as a therapeutic agent. *Biomol. Ther.* **26**, 225–241 (2018).
8. Singh, P. et al. Taurine deficiency as a driver of aging. *Science* **380**, eabn9257 (2023).
9. Wu, J. Y. & Prentice, H. Role of taurine in the central nervous system. *J. Biomed. Sci.* **17**, S1 (2010).
10. Liu, Q. R., Lopez-Corcuera, B., Nelson, H., Mandiyan, S. & Nelson, N. Cloning and expression of a cDNA encoding the transporter of taurine and beta-alanine in mouse brain. *Proc. Natl. Acad. Sci. USA* **89**, 12145–12149 (1992).

11. Preising, M. N. et al. Biallelic mutation of human SLC6A6 encoding the taurine transporter TAUT is linked to early retinal degeneration. *FASEB J.* **33**, 11507–11527 (2019).
12. Ansar, M. et al. Taurine treatment of retinal degeneration and cardiomyopathy in a consanguineous family with SLC6A6 taurine transporter deficiency. *Hum. Mol. Genet.* **29**, 618–623 (2020).
13. Wei, W. et al. PTER is a N-acetyltaurine hydrolase that regulates feeding and obesity. *Nature* **633**, 182–188 (2024).
14. Cao, T. et al. Cancer SLC6A6-mediated taurine uptake transactivates immune checkpoint genes and induces exhaustion in CD8(+) T cells. *Cell* **187**, 2288–2304 (2024).
15. Stary, D. & Bajda, M. Structural studies of the taurine transporter: A potential biological target from the GABA transporter subfamily in cancer therapy. *Int. J. Mol. Sci.* **25**, https://doi.org/10.3390/ijms25137339 (2024).
16. Stary, D. & Bajda, M. Taurine and creatine transporters as potential drug targets in cancer therapy. *Int. J. Mol. Sci.* **24**, https://doi.org/10.3390/ijms24043788 (2023).
17. Pramod, A. B., Foster, J., Carvelli, L. & Henry, L. K. SLC6 transporters: structure, function, regulation, disease association and therapeutics. *Mol. Asp. Med.* **34**, 197–219 (2013).
18. Tomi, M., Tajima, A., Tachikawa, M. & Hosoya, K. Function of taurine transporter (Slc6a6/TauT) as a GABA transporting protein and its relevance to GABA transport in rat retinal capillary endothelial cells. *Biochim. Biophys. Acta* **1778**, 2138–2142 (2008).
19. Yahara, T., Tachikawa, M., Akanuma, S., Kubo, Y. & Hosoya, K. Amino acid residues involved in the substrate specificity of TauT/SLC6A6 for taurine and gamma-aminobutyric acid. *Biol. Pharm. Bull.* **37**, 817–825 (2014).
20. Zhang, H. et al. Dimerization and antidepressant recognition at noradrenaline transporter. *Nature* **630**, 247–254 (2024).
21. Jayaraman, K. et al. SLC6 transporter oligomerization. *J. Neurochem.* **157**, 919–929 (2021).
22. Hamilton, P. J. et al. PIP2 regulates psychostimulant behaviors through its interaction with a membrane protein. *Nat. Chem. Biol.* **10**, 582–589 (2014).
23. Paul, A. & Shukla, D. Oligomerization of Monoamine Transporters. *Subcell. Biochem.* **104**, 119–137 (2024).
24. Anderluh, A. et al. Direct PIP(2) binding mediates stable oligomer formation of the serotonin transporter. *Nat. Commun.* **8**, 14089 (2017).
25. Anderluh, A. et al. Single molecule analysis reveals coexistence of stable serotonin transporter monomers and oligomers in the live cell plasma membrane. *J. Biol. Chem.* **289**, 4387–4394 (2014).
26. Das, A. K. et al. Dopamine transporter forms stable dimers in the live cell plasma membrane in a phosphatidylinositol 4,5-bisphosphate-independent manner. *J. Biol. Chem.* **294**, 5632–5642 (2019).
27. Periole, X., Zeppelin, T. & Schiott, B. Dimer interface of the human serotonin transporter and effect of the membrane composition. *Sci. Rep.* **8**, 5080 (2018).
28. Penmatsa, A., Wang, K. H. & Gouaux, E. X-ray structure of dopamine transporter elucidates antidepressant mechanism. *Nature* **503**, 85–90 (2013).
29. Coleman, J. A., Green, E. M. & Gouaux, E. X-ray structures and mechanism of the human serotonin transporter. *Nature* **532**, 334–339 (2016).
30. Srivastava, D. K. et al. Structure of the human dopamine transporter and mechanisms of inhibition. *Nature* **632**, 672–677 (2024).
31. Li, Y. et al. Dopamine reuptake and inhibitory mechanisms in human dopamine transporter. *Nature* **632**, 686–694 (2024).
32. Motiwala, Z. et al. Publisher correction: Structural basis of GABA reuptake inhibition. *Nature* **608**, E15 (2022).
33. Shahsavar, A. et al. Structural insights into the inhibition of glycine reuptake. *Nature* **591**, 677–681 (2021).
34. Hu, T. et al. Transport and inhibition mechanisms of the human noradrenaline transporter. *Nature* **632**, 930–937 (2024).
35. Nayak, S. R. et al. Cryo-EM structure of GABA transporter 1 reveals substrate recognition and transport mechanism. *Nat. Struct. Mol. Biol.* **30**, 1023–1032 (2023).
36. Richter, M., Moroniak, S. J. & Michel, H. Identification of competitive inhibitors of the human taurine transporter TauT in a human kidney cell line. *Pharm. Rep.* **71**, 121–129 (2019).
37. Hillenkamp, J., Hussain, A. A., Jackson, T. L., Cunningham, J. R. & Marshall, J. Taurine uptake by human retinal pigment epithelium: implications for the transport of small solutes between the choroid and the outer retina. *Invest. Ophthalmol. Vis. Sci.* **45**, 4529–4534 (2004).
38. Krishnamurthy, H. & Gouaux, E. X-ray structures of LeuT in substrate-free outward-open and apo inward-open states. *Nature* **481**, 469–474 (2012).
39. Han, X., Budreau, A. M. & Chesney, R. W. Ser-322 is a critical site for PKC regulation of the MDCK cell taurine transporter (pNCT). *J. Am. Soc. Nephrol.* **10**, 1874–1879 (1999).
40. Vogensen, S. B. et al. Structure activity relationship of selective GABA uptake inhibitors. *Bioorg. Med. Chem.* **23**, 2480–2488 (2015).
41. Zhu, A. et al. Molecular basis for substrate recognition and transport of human GABA transporter GAT1. *Nat. Struct. Mol. Biol.* **30**, 1012–1022 (2023).
42. Malinauskaite, L. et al. A mechanism for intracellular release of Na+ by neurotransmitter/sodium symporters. *Nat. Struct. Mol. Biol.* **21**, 1006–1012 (2014).
43. Wei, Y. et al. Transport mechanism and pharmacology of the human GlyT1. *Cell* **187**, 1719–1732 e1714 (2024).
44. Ramamoorthy, S. et al. Functional characterization and chromosomal localization of a cloned taurine transporter from human placenta. *Biochem. J.* **300**, 893–900 (1994).
45. Singh, S. K., Piscitelli, C. L., Yamashita, A. & Gouaux, E. A competitive inhibitor traps LeuT in an open-to-out conformation. *Science* **322**, 1655–1661 (2008).
46. Conti, F., Minelli, A. & Melone, M. GABA transporters in the mammalian cerebral cortex: localization, development and pathological implications. *Brain Res. Brain Res. Rev.* **45**, 196–212 (2004).
47. Yang, D. & Gouaux, E. Illumination of serotonin transporter mechanism and role of the allosteric site. *Sci. Adv.* **7**, eabl3857 (2021).
48. Tan, J. et al. Molecular basis of human noradrenaline transporter reuptake and inhibition. *Nature* **632**, 921–929 (2024).
49. Nielsen, J. C. et al. Structure of the human dopamine transporter in complex with cocaine. *Nature* **632**, 678–685 (2024).
50. Sitte, H. H., Farhan, H. & Javitch, J. A. Sodium-dependent neurotransmitter transporters: oligomerization as a determinant of transporter function and trafficking. *Mol. Inter.* **4**, 38–47 (2004).
51. Villumsen, K. R., Duelund, L. & Lambert, I. H. Acute cholesterol depletion leads to net loss of the organic osmolyte taurine in Ehrlich Lettre tumor cells. *Amino Acids* **39**, 1521–1536 (2010).
52. Goehring, A. et al. Screening and large-scale expression of membrane proteins in mammalian cells for structural studies. *Nat. Protoc.* **9**, 2574–2585 (2014).
53. Chen, X., Yin, Y., Zhou, Z., Li, T. & Zhu, Z. J. Development of a combined strategy for accurate lipid structural identification and quantification in ion-mobility mass spectrometry based untargeted lipidomics. *Anal. Chim. Acta* **1136**, 115–124 (2020).
54. Chen, X. et al. Trapped ion mobility spectrometry-mass spectrometry improves the coverage and accuracy of four-dimensional untargeted lipidomics. *Anal. Chim. Acta* **1210**, 339886 (2022).
55. Tu, J., Yin, Y., Xu, M., Wang, R. & Zhu, Z. J. Absolute quantitative lipidomics reveals lipidome-wide alterations in aging brain. *Metabolomics* **14**, 5 (2017).

56. Punjani, A., Rubinstein, J. L., Fleet, D. J. & Brubaker, M. A. cryoSPARC: algorithms for rapid unsupervised cryo-EM structure determination. *Nat. Methods* **14**, 290–296 (2017).
57. Goddard, T. D. et al. UCSF ChimeraX: Meeting modern challenges in visualization and analysis. *Protein Sci.* **27**, 14–25 (2018).
58. Emsley, P. & Cowtan, K. Coot: model-building tools for molecular graphics. *Acta Crystallogr. D. Biol. Crystallog.* **60**, 2126–2132 (2004).
59. Afonine, P. V. et al. Real-space refinement in PHENIX for cryo-EM and crystallography. *Acta Crystallogr. D. Struct. Biol.* **74**, 531–544 (2018).
60. Chen, V. B. et al. MolProbity: all-atom structure validation for macromolecular crystallography. *Acta Crystallogr. D. Biol. Crystallogr.* **66**, 12–21 (2010).
61. The PyMOL Molecular Graphics System. (2020).
62. Laskowski, R. A. & Swindells, M. B. LigPlot+: multiple ligand-protein interaction diagrams for drug discovery. *J. Chem. Inf. Model* **51**, 2778–2786 (2011).
63. Wallace, A. C., Laskowski, R. A. & Thornton, J. M. LIGPLOT: a program to generate schematic diagrams of protein-ligand interactions. *Protein Eng.* **8**, 127–134 (1995).

Acknowledgements

We thank the Cryo-Electron Microscopy Center at the Interdisciplinary Research Center on Biology and Chemistry, Shanghai Institute of Organic Chemistry, for the help with data collection. We thank ShanghaiTech Cryo-EM Imaging Facility for its assistance in data collection. We thank the Molecular and Cell Biology Core Facility (MCBCF) at the School of Life Science and Technology, ShanghaiTech University, for providing technical support. This work was supported by the Shanghai Lingang Laboratory (LG-QS-202203-03, to J.Y. and J.G.), Shanghai Basic Research Pioneer Project (J.Y.), startup grant of ShanghaiTech University (to J. G.) and Shanghai Pujiang Program (to J. G.).

Author contributions

J.Y., J.G. and D.Y. designed the project. Y.Z. performed the sample preparation for cryo-EM and biochemistry studies. Y.Z. and J.C. performed the uptake and kinetic assays. N.C. predicted a homology model. H.X. and Z.Z. carried out MS analysis. Y.Z. and J.Y. performed the cryo-EM data collection, data analysis and model building. J.Y., Y.Z., D.Y. and J.G. wrote the manuscript.

Competing interests

The authors declare no competing interests.

Additional information

Supplementary information The online version contains supplementary material available at https://doi.org/10.1038/s41467-025-60967-z.

Correspondence and requests for materials should be addressed to Dongxue Yang, Jingpeng Ge or Jie Yu.

Peer review information *Nature Communications* thanks Aravind Penmatsa who co-reviewed with Smruti Naikand Katsuhisa Inoue for their contribution to the peer review of this work. A peer review file is available.